Computers & Fluids 103 (2014) 86–99

Contents lists available at ScienceDirect

Computers & Fluids

journal homepage: www.elsevier.com/locate/compfluid

Sloshing impact simulation with material point method and its experimental validations ☆

J.G. Li [a], Y. Hamamoto [b], Y. Liu [a], X. Zhang [a,*]

[a] School of Aerospace, Tsinghua University, Beijing 100084, China
[b] Structural Strength Department, Research Laboratory, IHI Corporation, Yokohama 235-8501, Japan

ARTICLE INFO

Article history:
Received 24 January 2014
Received in revised form 24 June 2014
Accepted 26 July 2014
Available online 6 August 2014

Keywords:
Material point method
Contact algorithm
Liquid sloshing
Impact pressure

ABSTRACT

Liquid sloshing is usually associated with violent changes and breakups of free surfaces and strong fluid structure interactions. These phenomena present unique challenges for traditional computational fluid dynamics methods. In this paper, the material point method (MPM) is extended to solve the dynamic behavior of sloshing liquids in a moving container and a numerical scheme is developed to calculate impact pressure based on a contact algorithm over background grids. Moreover, a weakly compressible equation of state which employs an artificial sound speed is incorporated into the MPM to compute the pressure field of the liquid phase and a special scheme is employed to apply harmonic excitation to the particle-discretized container. The performance of the improved MPM in prediction of liquid impact pressure is verified by modeling a water block dropping test onto an aluminum plate. To further validate the proposed scheme, liquid sloshing experiments in a partially filled tank are conducted. The slosh-induced impact pressures on the vertical walls of the tank obtained from the MPM simulation are in good agreement with the experimental results.

1. Introduction

The phenomenon of liquid sloshing is a problem of practical interests in several industrial fields, such as mechanical engineering, marine engineering, in-land, aerospace transportation and civil engineering [1]. All containers that carry liquids must address the issue of sloshing. For example, ocean going liquefied natural gas (LNG) vessels may suffer from external wave impacts and inertial loads during the voyage, which can result in local damage as well as global collapse to the main hull structure, and can then further lead to leakage of fuel, or even overturn of the vessel. Sloshing pressure is also an important parameter in the assessment of safety of aeronautic and astronautic vehicles to prevent incidents induced by violent sloshing of liquefied fuel inside the fuel tank. The liquid oscillations in large storage tanks caused by earthquakes can produce tremendous impact pressure on the walls, which may result in serious casualties and economic losses. Hence, accurate predictions of the sloshing impact loads on offshore structures, space vehicles, storage tanks, water reservoirs, road vehicle tanks and ships are of great concern to engineers, designers, physicists, and mathematicians.

In the past decades, extensive mathematical formulations, experimental studies and more recently numerical simulations have been performed to deal with sloshing problems [2]. The early research efforts of this issue focused on two dimensional linear problems in containers with simple geometry, which can be solved by analytical methods [3]. With the advent of the modern theory of nonlinear dynamics, nonlinear models [4–7] with viscous damping based on potential flow theory have been developed to further study both two dimensional and three dimensional complex surface dynamic phenomena of sloshing liquid in moving containers. However, these researches are usually valid for simple cases with linear or weakly nonlinear liquid sloshing dynamics, and analytical techniques for predicting large-amplitude sloshing are still not fully developed. Furthermore, liquid sloshing dynamics generally involve strong nonlinear phenomena such as wave breaking, particle splash, and jet flow. Thus, taking into account all these factors analytically is extremely difficult.

Sloshing pressure is an important parameter in an assessment of safety of hull design when ships containing liquids sail through rough seas. In order to find the characteristics of the impact pressure [8], researchers have to conduct large-scale experiments (even full scale tests) to reflect what happens in the tank and find

☆ Supported by the Tsinghua-IHI Cooperation Project (92), the National Natural Science Foundation of China (11272180), and Specialized Research Fund for the Doctoral Program of Higher Education (SRFDP) of Chinese Ministry of Education (20110002120045).

* Corresponding author.
E-mail address: xzhang@tsinghua.edu.cn (X. Zhang).

http://dx.doi.org/10.1016/j.compfluid.2014.07.025
0045-7930/

phenomena which only occur in large-size tanks due to the three dimensional effects since there is no proper scaling law [9] which can transfer the model results to prototype conditions perfectly, when it comes to impact loads. For these reasons, laboratory experiments usually have problems of long experiment cycle and high cost.

As mentioned above, experimental works are generally expensive and sometimes certain physical phenomena related to liquid sloshing cannot be scaled in a practical experimental setup. Recently more and more researches on liquid sloshing are focused on numerical simulations with the fast advancement of the computer hardware and numerical algorithms. A number of researchers have provided comprehensive reviews on the problem of liquid sloshing, and the related two dimensional and three dimensional numerical simulation methods [10–12]. Most of the numerical simulations are focused on Eulerian and Arbitrary Lagrangian–Eulerian grid-based methods, such as finite difference method (FDM) [13,14], finite volume method (FVM) [15,16], finite element method (FEM) [17,18] and boundary element method (BEM) [5,6]. As a complex fluid motion, sloshing processes usually involve the complex variation of liquid surface, violent turbulence and vortex, as well as the strong coupling between the fluid and container walls, which bring many difficulties to traditional grid-based numerical methods when dealing with liquid sloshing problems. These goals and simulation challenges have led to the development of hybird methods building upon the work of others. For example, traditional FDM and FVM often require special algorithms such as volume-of-fluid (VOF) method [19,20] or level-set method [21] to capture changing surfaces or moving interfaces for certain classes of problems in liquid sloshing dynamics.

Besides the grid-based methods, particle methods (or meshfree methods) in which fluid particles are followed in a Lagrangian manner provide innovative alternatives to solve complex fluid dynamics problems such as liquid sloshing dynamics. To name a few, Idelsohn et al. [22] developed the PFEM (particle finite element method) to solve incompressible flows with free-surfaces and breaking waves. Koshizuka et al. [23] and Lee et al. [24] used the MPS (moving particle semi-implicit method) to study violent free surface motions and impact loads. Nestor et al. [25] established the FVPM (finite volume particle method) for meshfree simulation of viscous flow problems in engineering.

More recently, smoothed particle hydrodynamics (SPH) is being increasingly used to simulate fluid motions for its simple calculation and easy implementation [26]. The SPH method was originally developed in the late 1970s to solve astrophysical problems in three-dimensional open space [27]. In 1990s, Libersky et al. [28] extended it to high strain hydrodynamics problems with material strength. Since then, SPH has been extensively studied and extended to different problems in science and engineering, including high explosive detonation and explosion [29,30], high velocity impact and penetration [31], multi-phase [32], free surface flows [33,34] and sloshing type problems [35,36]. After being continuously improved, SPH was extended first to weakly compressible flows [37,38], then to strongly compressible [39] and truly incompressible hydrodynamics [40] as well. In SPH, a series of particles possessing individual material properties are used to represent the state of a system and these particles are capable of moving in the space according to internal particle interactions and external forces. Since the collective movement of those particles is similar to the movement of a liquid or gas flow, SPH can give a very good description of violent fluid motion phenomenon like sloshing. As a purely Lagrangian meshfree method, SPH can naturally track material interfaces, free surfaces and moving boundaries, and the history of flow field variables (such as pressure, velocity, density) can be easily obtained by approximating the governing equations which are discretized on the particles. However, special care are required to the solid boundary treatment and the low accuracy of the pressure measurement on solid walls when dealing with fluid motions [2]. Moreover, a neighboring particles search is needed at each time step, which makes the SPH computation much expensive.

Among all kinds of particle-oriented methods, the material point method (MPM) [41,42] is an extension to solid mechanics problems of a hydrodynamics code named FLIP [43]. In MPM, the material domain is discretized with a set of Lagrangian material points (particles), each with local mass and other state variables in order to model history-dependent behaviors. A spatial background grid that provides an Eulerian description of the material domain is predefined to calculate the gradient and integrate the momentum equation. At each time step, the particles are rigidly attached to background grid and move with the grid. Kinematic variables are firstly mapped from particles to grid nodes to establish the momentum equations on background grid, and the solutions of the momentum equation are then mapped from grid nodes back to particles to update their velocities and positions. At the end of each time step, the deformed grid is discarded and a new regular computational grid is set up for the next time step so that there is no mesh distortion or element entanglement associated with the FEM, while numerical dissipation normally associated with Eulerian methods is reduced.

MPM combines the advantages of both Lagrangian and Eulerian methods [44]. These features make it fairly attractive in modeling liquid sloshing dynamics, which is usually associated with changes of free surfaces and violent fluid–structure interactions, wave interactions with other structures especially in ocean and coastal hydrodynamics and offshore engineering. Typical applications of MPM in this area include fluid–structure interaction [45–47], ice dynamics [48], multiphase flows [49]. According to the Courant–Friedrich–Levy (CFL) condition, the critical time step size in MPM depends on cell size of the spatial background grid, rather than the particle space in SPH, so that the time step used in MPM is much larger than that of SPH. Furthermore, there is no neighboring particles search which is very time consuming. Therefore, MPM is much more efficient than SPH [50–52].

This paper aims at predicting sloshing impact pressure by extending MPM to the simulation of dynamic behaviors of fluid under external excitations. In this study, the liquid medium is assumed to be weakly compressible by employing an artificial equation of state (EOS) to relate the pressure and density, which is the most commonly used procedure in particle-based method. A novel algorithm based on contact algorithms proposed by Bardenhagen et al. [53,54] and Huang et al. [55] is then developed for accurate calculation of impact pressure over the background grid while a special scheme is employed to apply harmonic excitation to the particle-discretized container.

The remaining parts of the paper are organized as follows. Section 2 gives a brief description of the mathematical formulation of MPM and its time integration scheme. Several numerical strategies for the simulation of liquid sloshing dynamics are presented in Section 3. In Section 4, the improved MPM is first verified by a water block dropping test and then validated by fluid sloshing experiments in a partially filled tank. Numerical results are in good agreement with experimental observations. Finally, conclusions are drawn in Section 5.

2. MPM formulations

The MPM discretizes a material domain by a set of particles, as shown in Fig. 1. Each particle carries the position, velocity, mass, density, stress, strain and all other internal state variables required for the constitutive model. A background computational grid is used to calculate the gradient terms.

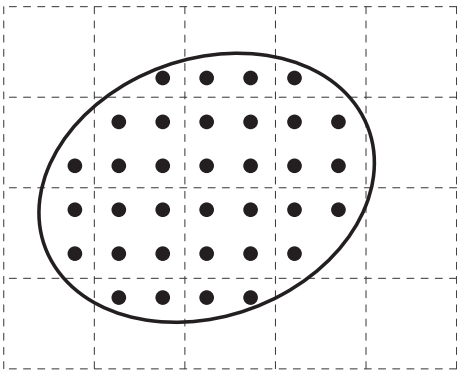

Fig. 1. Typical particle discretization of a two dimensional material domain. Solid line denotes the boundary of the material domain, solid dots are particles and dash lines represent the background computational grid.

The momentum balance equation in the updated Lagrangian description is stated as

$$\rho \frac{d\boldsymbol{v}}{dt} = \nabla \cdot \boldsymbol{\sigma} + \rho \boldsymbol{b} \tag{1}$$

where $\rho(\boldsymbol{x},t)$ is the mass density, $\boldsymbol{v}(\boldsymbol{x},t) = d\boldsymbol{u}(\boldsymbol{x},t)/dt$ is the velocity, $\boldsymbol{\sigma}(\boldsymbol{x},t)$ is the Cauchy stress tensor, and $\boldsymbol{b}(\boldsymbol{x},t)$ is the specific body force. The vector $\boldsymbol{x}$ is the Cartesian coordinate of a particle at time t.

In order to obtain a solution for Eq. (1), boundary conditions

$$\boldsymbol{\sigma}(\boldsymbol{x},t)\cdot\boldsymbol{n}|_{\Gamma_t} = \bar{\boldsymbol{t}}(t), \quad \boldsymbol{u}(\boldsymbol{x},t)|_{\Gamma_u} = \bar{\boldsymbol{u}}(t) \tag{2}$$

and initial conditions

$$\boldsymbol{u}(\boldsymbol{x},0) = \boldsymbol{u}_0(\boldsymbol{x}), \quad \boldsymbol{v}(\boldsymbol{x},0) = \boldsymbol{v}_0(\boldsymbol{x}) \tag{3}$$

are required, where Γ_t is the part of the boundary with a prescribed traction vector $\bar{\boldsymbol{t}}$, Γ_u is the boundary with a prescribed displacement $\bar{\boldsymbol{u}}$, $\boldsymbol{n}$ is the outward normal to the surface Γ_t, $\boldsymbol{u}_0(\boldsymbol{x})$ and $\boldsymbol{v}_0(\boldsymbol{x})$ are the initial displacement and velocity.

The Galerkin weak form of Eq. (1) can be stated as

$$\int_V \rho\ddot{\boldsymbol{u}}\cdot\boldsymbol{w}dV + \int_V \boldsymbol{\sigma} : \nabla\boldsymbol{w}dV - \int_V \rho\boldsymbol{w}\cdot\boldsymbol{b}dV - \int_{\Gamma_t} \boldsymbol{w}\cdot\bar{\boldsymbol{t}}d\Gamma = 0 \tag{4}$$

where $\boldsymbol{w} \in \Re_0$, $\Re_0 = \{\boldsymbol{w}|\boldsymbol{w}\in C^0, \boldsymbol{w}|_{\Gamma_u} = 0\}$ denotes the test function, V is the current configuration of the continuum.

Since the whole domain is described with n_p particles, the mass density can be approximated as

$$\rho(\boldsymbol{x},t) = \sum_{p=1}^{n_p} m_p \delta(\boldsymbol{x} - \boldsymbol{x}_p^t) \tag{5}$$

where m_p is the mass of particle p, δ is the Dirac delta function, $\boldsymbol{x}_p^t$ is the current position of particle p at time t. Substituting Eq. (5) into Eq. (4) converts the integrals to the sums of quantities evaluated at the particles, namely

$$\sum_{p=1}^{n_p} m_p\ddot{\boldsymbol{u}}_p\cdot\boldsymbol{w}_p + \sum_{p=1}^{n_p}\frac{m_p}{\rho_p}\boldsymbol{\sigma}_p : \nabla\boldsymbol{w}_p - \sum_{p=1}^{n_p} m_p\boldsymbol{b}_p\cdot\boldsymbol{w}_p - \sum_{p=1}^{n_p}\frac{m_p}{\rho_p h}\bar{\boldsymbol{t}}_p\cdot\boldsymbol{w}_p = 0 \tag{6}$$

with h being the thickness of the boundary layer. In Eq. (6), $\ddot{\boldsymbol{u}}_p$ is the acceleration of particle p.

In three dimensional MPM, a background grid is constructed by using 8-node hexahedron cells. In all notations, the subscript index p is associated with particles and subscript index I is associated with background grid nodes. For the 8-node cell, the nodal shape functions are given by

$$N_I = \frac{1}{8}(1+\xi\xi_I)(1+\eta\eta_I)(1+\zeta\zeta_I), \quad I = 1,2,\ldots,8 \tag{7}$$

where ξ_I, η_I and ζ_I are the natural coordinates (±1) at node I. The displacements of any particle in a cell can then be represented by the nodal displacements $\boldsymbol{u}_I$ as

$$\boldsymbol{u}_p = \sum_{I=1}^{n_g} N_{Ip}\boldsymbol{u}_I \tag{8}$$

where $N_{Ip} = N_I(\boldsymbol{x}_p)$ is the value of shape function associated with node I evaluated at particle p, n_g is the total number of nodes of the background mesh. The test function $\boldsymbol{w}$ has the same form, namely

$$\boldsymbol{w}_p = \sum_{I=1}^{n_g} N_{Ip}\boldsymbol{w}_I \tag{9}$$

where $\boldsymbol{w}_I$ is the value of test function evaluated at node I.

Substituting Eqs. (7)–(9) into Eq. (6) and invoking the arbitrariness of $\boldsymbol{w}_I (I \notin \Gamma_v)$ yields

$$\dot{\boldsymbol{p}}_I = \boldsymbol{f}_I^{\text{int}} + \boldsymbol{f}_I^{\text{ext}}, \quad I \notin \Gamma_v \tag{10}$$

where

$$\boldsymbol{p}_I = \sum_{J=1}^{n_g} m_{IJ}\dot{\boldsymbol{u}}_J = m_I\dot{\boldsymbol{u}}_I \tag{11}$$

is the momentum of grid node I,

$$m_{IJ} = \sum_{p=1}^{n_p} m_p N_{Ip}N_{Jp}, \quad m_I = \sum_{p=1}^{n_p} m_p N_{Ip} \tag{12}$$

are the mass matrix and lumped mass matrix respectively,

$$\boldsymbol{f}_I^{\text{ext}} = \sum_{p=1}^{n_p} m_p N_{Ip}\boldsymbol{b}_p + \sum_{p=1}^{n_p} N_{Ip}\bar{\boldsymbol{t}}_p h^{-1}\frac{m_p}{\rho_p} \tag{13}$$

is the external nodal force vector,

$$\boldsymbol{f}_I^{\text{int}} = -\sum_{p=1}^{n_p}\frac{m_p}{\rho_p}\boldsymbol{\sigma}_p\cdot\boldsymbol{G}_{Ip} \tag{14}$$

is the internal nodal force vector, and $\boldsymbol{G}_{Ip} = \nabla N_I|_{\boldsymbol{x}_p}$ is the gradient of the shape function.

The central difference method is employed to solve Eq. (10) explicitly with the variable time step, Δt^n, satisfying the CFL condition

$$\Delta t^n \leqslant \Delta t_{\text{cr}} = \frac{d_c}{\max_p(c_s + |\boldsymbol{v}_p|)} \tag{15}$$

where d_c is the cell size of the background grid, c_s is the sound speed. The nodal momentum is updated with a leapfrog scheme by (shown in Fig. 2)

$$\boldsymbol{p}_I^{n+1/2} = \boldsymbol{p}_I^{n-1/2} + (\boldsymbol{f}_I^{n,\text{int}} + \boldsymbol{f}_I^{n,\text{ext}})\Delta t^n \tag{16}$$

where $\Delta t^n = t^{n+1/2} - t^{n-1/2} = \frac{1}{2}(\Delta t^{n-1/2} + \Delta t^{n+1/2})$, $\Delta t^{n+1/2} = t^{n+1} - t^n$. It should be noted that the superscript n indicates the value of a variable at time t^n.

Based on the three-dimensional explicit material point method code MPM3D® [56], a step-by-step modified update stress last (MUSL) [42] MPM scheme is described as follows.

1. At the beginning of time step t^n, the mass and momentums of particles are mapped onto the background grid to calculate the nodal mass m_I^n and momentum $\boldsymbol{p}_I^{n-1/2}$, namely

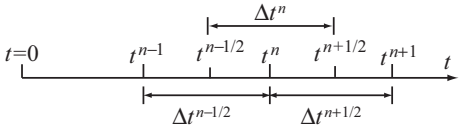

Fig. 2. The leapfrog central difference method.

$$m_I^n = \sum_{p=1}^{n_p} m_p N_{Ip}^n \tag{17}$$

$$\boldsymbol{p}_I^{n-1/2} = \sum_{p=1}^{n_p} m_p \boldsymbol{v}_p^{n-1/2} N_{Ip}^n \tag{18}$$

where m_p and $\boldsymbol{v}_p^{n-1/2}$ are the particle mass and current velocity vector respectively.

2. Apply essential boundary conditions to the fixed grid nodes, that is

$$\boldsymbol{p}_I^{n-1/2} = \boldsymbol{0} \tag{19}$$

3. Compute the nodal force vector $\boldsymbol{f}_I^n$,

$$\boldsymbol{f}_I^n = \boldsymbol{f}_I^{n,\text{int}} + \boldsymbol{f}_I^{n,\text{ext}} \tag{20}$$

where $\boldsymbol{f}_I^{n,\text{int}}$ and $\boldsymbol{f}_I^{n,\text{ext}}$ are obtained from Eqs. (13) and (14) respectively. For grid nodes on the fixed boundary, let $\boldsymbol{f}_I^n = 0$.

4. Update the grid nodal momentum by

$$\boldsymbol{p}_I^{n+1/2} = \boldsymbol{p}_I^{n-1/2} + \boldsymbol{f}_I^n \Delta t^n \tag{21}$$

5. Update the particle velocity and position, respectively, by

$$\boldsymbol{v}_p^{n+1/2} = \boldsymbol{v}_p^{n-1/2} + \sum_{I=1}^{n_I} \frac{\boldsymbol{f}_I^n}{m_I^n} N_{Ip}^n \Delta t^n \tag{22}$$

$$\boldsymbol{x}_p^{n+1} = \boldsymbol{x}_p^n + \sum_{I=1}^{n_I} \frac{\boldsymbol{p}_I^{n+1/2}}{m_I^n} N_{Ip}^n \Delta t^n \tag{23}$$

6. Recalculate the nodal momentum from the updated particle velocity

$$\boldsymbol{p}_I^{n+1/2} = \sum_{p=1}^{n_p} m_p \boldsymbol{v}_p^{n+1/2} N_{Ip}^n \tag{24}$$

7. Calculate the strain and vorticity increment of a particle by

$$\Delta \boldsymbol{\varepsilon}_p^{n+1/2} = \frac{1}{2} \sum_{I=1}^{n_g} \left[\left(\boldsymbol{G}_{Ip}^n \boldsymbol{v}_I^{n+1/2} \right)^{\mathrm{T}} + \boldsymbol{G}_{Ip}^n \boldsymbol{v}_I^{n+1/2} \right] \Delta t^{n+1/2} \tag{25}$$

$$\Delta \boldsymbol{\omega}_p^{n+1/2} = \frac{1}{2} \sum_{I=1}^{n_g} \left[\left(\boldsymbol{G}_{Ip}^n \boldsymbol{v}_I^{n+1/2} \right)^{\mathrm{T}} - \boldsymbol{G}_{Ip}^n \boldsymbol{v}_I^{n+1/2} \right] \Delta t^{n+1/2} \tag{26}$$

where the nodal velocity are determined by $\boldsymbol{v}_I^{n+1/2} = \boldsymbol{p}_I^{n+1/2} / m_I^n$. Then update the particle density

$$\rho_p^{n+1} = \rho_p^n / (1 + \mathrm{tr}(\Delta \boldsymbol{\varepsilon}_p^{n+1/2})) \tag{27}$$

and input the strain and vorticity increment into a material constitutive law to obtain the updated particle stresses

$$\boldsymbol{\sigma}_p^{n+1} = \boldsymbol{\sigma}_p^n + \Delta \boldsymbol{\sigma}_p^{n+1/2} (\Delta \boldsymbol{\varepsilon}_p^{n+1/2}, \Delta \boldsymbol{\omega}_p^{n+1/2}) \tag{28}$$

For an incompressible Newtonian fluid like water, the deviatoric stress tensor $\boldsymbol{\tau}$ may be expressed as a function of the velocity field through the dynamical molecular viscosity μ by

$$\boldsymbol{\tau}_p^{n+1} = \mu \sum_{I=1}^{n_g} \left[\left(\boldsymbol{G}_{Ip}^n \boldsymbol{v}_I^{n+1/2} \right)^{\mathrm{T}} + \boldsymbol{G}_{Ip}^n \boldsymbol{v}_I^{n+1/2} \right] \tag{29}$$

8. Discard and reinitialize the grid for the next time step.

3. Numerical strategies for sloshing problems

3.1. Incompressible flow with artificial equation of state

In the particle method, an artificial compressibility technique is usually used to model the incompressible flow as a weakly compressible flow. Hence, slight compressibility is allowed through the following relation

$$\frac{\partial p}{\partial t} + \rho c^2 \nabla \cdot \boldsymbol{v} = 0 \tag{30}$$

which is derived from the mass conservation by assuming an incompressible liquid with artificial compressibility. The artificial compressibility considers that every theoretically incompressible fluid is actually compressible. It is therefore feasible to use a quasi-incompressible EOS to model the incompressible flow by an artificial relation between the pressure and the fluid density. In this paper, the artificial EOS [57]

$$p = \rho c^2 \tag{31}$$

is used, where c is the numerical sound speed which is normally taken smaller than reality but ten times higher than the maximum fluid velocity in order to reduce the density fluctuation down to 1%. In this way, a good compromise between efficiency and accuracy can be obtained by allowing larger time steps and still ensuring approximate incompressible behavior for the fluid. Monaghan [37] argued that the relative density variation δ is related to the fluid bulk velocity and sound speed in the following way

$$\delta = \frac{\Delta \rho}{\rho_0} = \frac{|\rho - \rho_0|}{\rho_0} = \frac{v_f^2}{c^2} = M^2 \tag{32}$$

where ρ_0 is the reference density, $\Delta\rho$ is the absolute density variation, v_f is the fluid bulk velocity and M is the Mach number respectively.

The advantage of artificial EOS is that it is easy to program since the pressure is obtained from Eq. (31) explicitly. However, some drawbacks appear. Firstly, this scheme requires a very small time step associated with a numerical speed of sound which is at least ten times higher than the maximum fluid velocity. Secondly, small density fluctuations always cause significant unphysical high-frequency pressure oscillations that are often numerically filtered out as part of a simulation.

In MPM, the material domain is discretized with a set of Lagrangian particles. At each time step, the particles are rigidly attached to the background grid and move along with it. The background grid serves as a finite element discretization to the material domain, on which the momentum equations are solved. Similar to FEM, the natural boundary condition is satisfied automatically in MPM. Therefore, the free surface is captured by the Lagrangian particles without any additional treatment.

3.2. Contact method in MPM

Contact phenomena are widely observed in a broad range of engineering fields. Since a single-valued velocity field is used to update the positions of particles, the no-slip contact between two different bodies can be handled automatically without any extra cost using the original MPM and the contact surface need not to be detected. Furthermore, Bardenhagen et al. [53,54] extended the original MPM to the friction (or slip) contact between deformable solid bodies, which allows Coulomb friction and slip at contact nodes. The contact force between bodies is obtained from the relative nodal velocity at the contact surface. To release the no-slip contact algorithm in MPM, a global multi-mesh mapping scheme was proposed by Hu and Chen [58]. In the multi-mesh environment, each material lies in an individual background grid rather than in the common one. Therefore, the algorithm occupies vast memory if there are a lot of bodies. To solve this problem, Ma and Zhang et al. [56] proposed a local multi-mesh contact algorithm, which creates individual grid for each body only at

contacted nodes and needs much less memory than the global multi-mesh scheme.

The impenetrability constraints need to be imposed only when the bodies are approaching (Fig. 3). If the momenta of two bodies are projected on to the same node I, the contact between bodies r and s may occur when

$$(\boldsymbol{v}_I^r - \boldsymbol{v}_I^s)\cdot \boldsymbol{n}_I^r > 0 \tag{33}$$

where $\boldsymbol{n}_I^b\,(b = r,s)$ is the outward unit normal vector of body b at node I along the boundary, $\boldsymbol{v}_I^b$ is the nodal velocity.

Bardenhagen et al. [54] proposed a method to compute the unit surface normal vector with the gradient of the nodal mass m_I^b in the individual body, that is

$$\boldsymbol{n}_I^b = \frac{\sum \boldsymbol{G}_{Ip} m_p^b}{|\sum \boldsymbol{G}_{Ip} m_p^b|}, \quad b = r,s \tag{34}$$

where m_p^b is the mass of particle p in body b. However, the normal vectors given by Eq. (34) cannot guarantee the collinearity condition

$$\boldsymbol{n}_I^r + \boldsymbol{n}_I^s = 0 \tag{35}$$

which should be satisfied at the contact surface. Non-collinearity of normal vectors at contact surface will lead to the non-conservation of momentum in the contact computation. To solve this problem, Huang and Zhang et al. [55] proposed a modification to determine the surface normal vectors $\boldsymbol{n}_I^b$ which satisfies the collinearity condition Eq. (35) at the contact surface. In this paper, the contact normal vector is set to be consistent with the normal of solid surface when hit by liquid medium.

A more accurate solution in MPM is obtained using the nodal momentum rather than the nodal velocity. The fundamental idea of the contact algorithm [59] is illustrated in detail below.

In each time step, the bodies are first integrated independently to obtain the trial values of nodal variables, as if they were not in contact. Integrating the momentum equation of bodies independently gives the trial nodal momenta

$$\bar{\boldsymbol{p}}_I^{b,n+1/2} = \boldsymbol{p}_I^{b,n-1/2} + \Delta t^n \boldsymbol{f}_I^{b,n} \tag{36}$$

At the end of the time step, a body would penetrate its neighbor body in the vicinity of grid node I when

$$(\bar{\boldsymbol{v}}_I^{r,n+1/2} - \bar{\boldsymbol{v}}_I^{s,n+1/2})\cdot \boldsymbol{n}_I^{r,n} > 0 \tag{37}$$

where $\bar{\boldsymbol{v}}_I^{b,n+1/2} = \bar{\boldsymbol{p}}_I^{b,n+1/2} \big/ m_I^{b,n}$ is the trial nodal velocity vector of body b, which should be corrected so that the impenetrability condition

$$(\boldsymbol{v}_I^{r,n+1/2} - \boldsymbol{v}_I^{s,n+1/2})\cdot \boldsymbol{n}_I^{r,n} = 0 \tag{38}$$

is satisfied. Otherwise, the trial values of nodal velocities represent the true solution, let $\boldsymbol{v}_I^{b,n+1/2} = \bar{\boldsymbol{v}}_I^{b,n+1/2}$.

Once body r and s contact, the corrected nodal momenta are obtained by

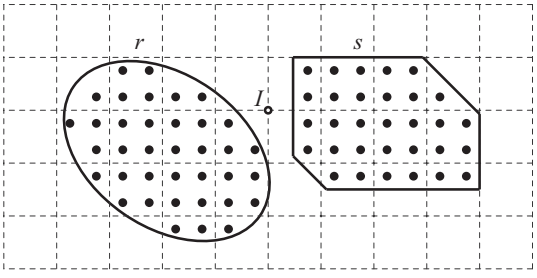

Fig. 3. Two bodies (r and s) may contact at node I when they are approaching.

$$\boldsymbol{p}_I^{b,n+1/2} = \bar{\boldsymbol{p}}_I^{b,n+1/2} + \Delta t^n \boldsymbol{f}_I^{\mathrm{nor},n} \tag{39}$$

Substituting Eq. (39) into Eq. (38) gives the normal contact force

$$f_I^{\mathrm{nor},n} = \frac{(m_I^{r,n}\bar{\boldsymbol{p}}_I^{s,n+1/2} - m_I^{s,n}\bar{\boldsymbol{p}}_I^{r,n+1/2})\cdot \boldsymbol{n}_I^{r,n}}{(m_I^{r,n} + m_I^{s,n})\Delta t^n} \tag{40}$$

The contact algorithm has been finished if there is no friction between bodies. The tangential contact force, or friction, can be determined according to the Coulomb friction model, which can be written as

$$f_I^{\mathrm{fric},n} = \min(\mu f_I^{\mathrm{nor},n}, f_I^{\tan,n}) \tag{41}$$

where

$$f_I^{\tan,n} = \frac{(m_I^{r,n}\bar{\boldsymbol{p}}_I^{s,n+1/2} - m_I^{s,n}\bar{\boldsymbol{p}}_I^{r,n+1/2})\cdot \boldsymbol{s}_I^{r,n}}{(m_I^{r,n} + m_I^{s,n})\Delta t^n} \tag{42}$$

with $\boldsymbol{s}_I^r$ being the unit tangential at node I along the boundary of body r, μ is the friction coefficient.

3.3. Impact pressure calculation based on the contact algorithm

The slosh-induced impulsive loads on tank walls are of particular interest when studying sloshing flows. However, sloshing impact pressure is often influenced by many parameters of liquid, gas and structure involved in the impact, such as the local geometry, gas/liquid density, viscosity, environmental temperature and atmospheric pressure, surface tension, compressibility, structure elasticity, and local bubbles. High impact pressure is strictly localized in the space and the time, being very sensitive to the local effects. Moreover, sloshing is a highly stochastic phenomenon. This highly nonlinear behavior may cause different impact pressures though drive motions are the same. Experiments show that even under harmonic oscillations, the pressure variation is neither harmonic nor periodic because the magnitude of the pressure peaks vary from cycle to cycle [2].

Consequently, the accurate prediction of hydrodynamic impact is a very challenging task and careful treatments are essential for the MPM simulation. Fluid slamming denotes the impact between a liquid surface and a solid boundary (e.g., a tank bulkhead). Since impact pressure occurs when the liquid collides with the wall or ceiling, a special numerical scheme based on the aforementioned contact algorithm is proposed to predict the impact pressure.

Impact may occur when two bodies (r and s) are approaching. To calculate the impact pressure at the gauge located on a specified body surface (shown in Fig. 4(a)), the following steps are proposed in the framework of MPM3D® [56]. At the beginning, the particle p nearest to the gauge point on the surface is found out. This particle will move along with the body and record all of the state variables including the local impact pressure. At each time step, the cell where the particle p is located in is firstly found out and then its n_{cn} influencing nodes are obtained. For each contact node, the normal contact force f_I^{nor} at node I is computed using Eq. (40), and the normal contact force divided by the influencing area A_I is considered to be the nodal impact pressure, that is, $p_I^{\mathrm{nor}} = f_I^{\mathrm{nor}}/A_I$. Finally, the impact pressure at particle p is updated by mapping from the influencing nodes, that is

$$p_p^n = \sum_{I=1}^{n_{cn}} \widetilde{N}_{Ip} p_I^{\mathrm{nor},n} \tag{43}$$

where

$$\widetilde{N}_I = \frac{1}{4}(1+\xi\xi_I)(1+\eta\eta_I), \quad I = 1,2,\ldots,4 \tag{44}$$

is the shape function of a quadrilateral element. The above steps to solve the impact pressure are illustrated in Algorithm 1.

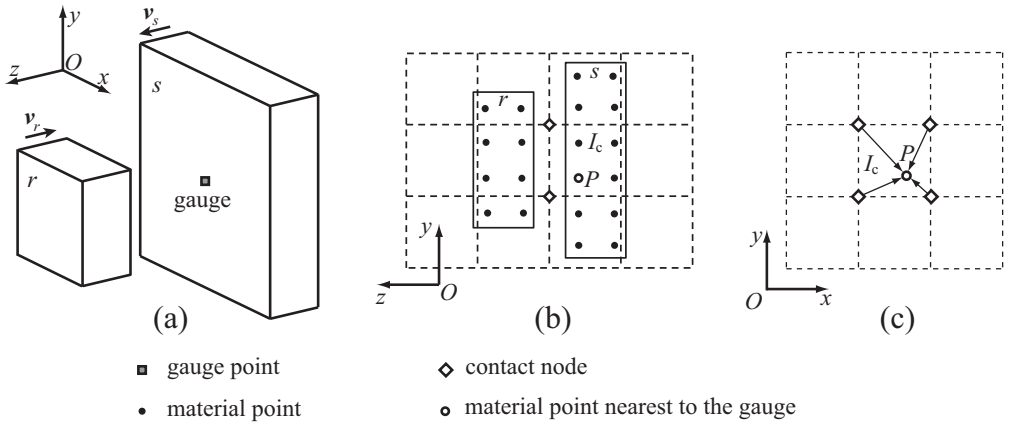

Fig. 4. Strategy to calculate the impact pressure in framework of MPM.

Algorithm 1. Steps to calculate the impact pressure

1. At the initial time step $t = 0$ find the particle p nearest to the gauge
2. At the time step t^n
   (a) find the cell I_c where the particle p is located in
   (b) find the contact nodes of cell I_c
   (c) **for** $I = 1{:}n_{cn}$ **do**
   compute normal contact force $f_I^{\text{nor},n}$
   compute nodal impact pressure $p_I^{\text{nor},n}$
   (d) update impact pressure p_p^n at particle p

To validate the accuracy of the above contact algorithm, the impact of two symmetric bars is investigated. In this simulation, the initial gap between the two bars is set as 1 mm, and the friction coefficient is zero. The length of the bar is 21 mm and the area is 3×3 mm^2. Two bars are traveling with an equal and opposite velocity of 100 m/s towards each other. Elastic material law is applied for both bars with Young's modulus $E = 6.5 \times 10^4$ MPa, Poisson's ratio $v = 0$ and density $\rho = 2.75$ g/cm^3. The discretization of the two bars is shown in Fig. 5. Plane strain assumption is applied along the sides of the model with symmetrical boundary conditions, which result in one-dimensional wave propagation in the bars. The grid cell size is set as 0.5 mm and the initial particle space is 0.25 mm.

The analytical impact pressure in this problem is given by

$$p = \frac{v_1 + v_2}{\frac{1}{\rho_1 c_1} + \frac{1}{\rho_2 c_2}} = 1.34 \times 10^3 \text{ MPa} \tag{45}$$

where $c_i = \sqrt{E_i/\rho_i}$ ($i = 1, 2$).

Fig. 6 compares the time history of the contact pressure in the bars obtained by MPM and one dimensional analytical solution, which shows that MPM results are in good agreement with the analytical solution obtained by Eq. (45).

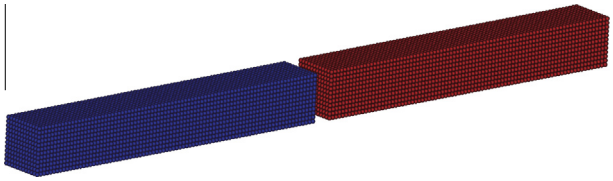

Fig. 5. MPM discretization of two impacting bars.

3.4. Sloshing loads assignment procedure

In our sloshing experiments, the tank platform fixed on the base frame was driven by a motor controlling the rotational/swaying motions. As the tank moves, it supplies energy to sustain the fluid motion. Similarly in MPM simulation, the tank is assigned an external excitation to move in accordance with the experimental design. In this paper, two kinds of excitations, $\alpha(t) = \alpha_0 \sin(\omega_r t)$ for the roll case while $s(t) = s_0 \sin(\omega_s t)$ for the sway case, are studied. Since the deformation of the tank undergoing sloshing is tiny, the tank could be considered as rigid during the MPM simulation. Therefore, for all the particles of the tank, the new particle velocity in Eq. (22) is updated based on the assigned rigid body motion. For the roll excitation illustrated in Fig. 7, the new particle velocity is updated by $v_p(t) = \Omega_r(t) r_p$ where $\Omega_r(t) = \dot{\alpha}(t) = \Omega_r^0 \sin(\omega_r t + \theta_0)$ is the angular velocity. For the sway case, the new particle velocity is updated by $v_p(t) = \dot{s}(t) = v_s^0 \sin(\omega_s t + \theta_0)$. In this paper, the equilibrium position is chosen at the initial configuration, therefore, the value of θ_0 is set as $\pi/2$. As a final step, the new position of each wall particle is updated by Eq. (23) based on the assigned particle velocity.

4. Numerical investigations and experimental validations

4.1. Water block impacting onto a plate

To validate the performance of the mathematical model and MPM scheme in the prediction of liquid slamming, a water block impacting onto a plate is first simulated. In Edahiro's experiment [60], a cylindrical water block was dropped onto a horizontal plate from rest at an initial height $H_0 = 500$ mm, as shown in Fig. 8. The

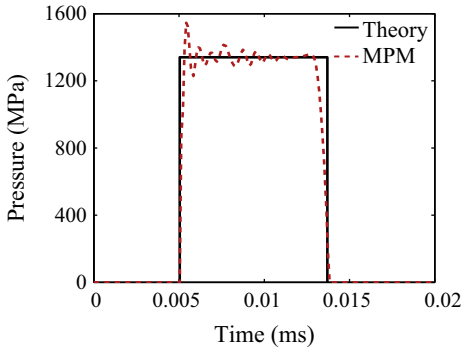

Fig. 6. Time history of impact pressure.

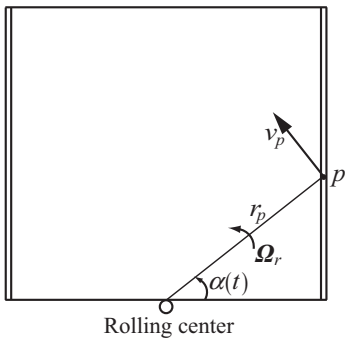

Fig. 7. The particle-discretized container under harmonic excitation.

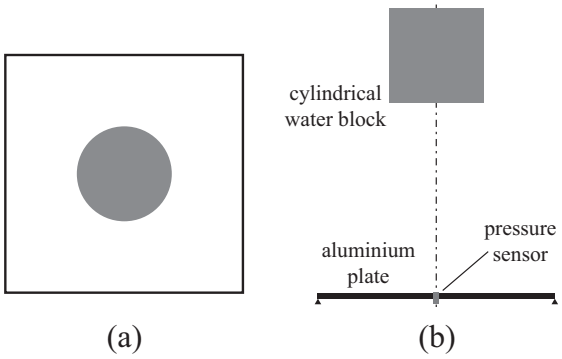

Fig. 8. Sketch of the experiment device: (a) top view; (b) side view.

water was initially kept in a circular tube, which kept the inner water block with a diameter and height of 100 mm. An aluminum plate with the dimension of 250 mm × 250 mm × 20 mm was located at the bottom and a pressure sensor was fixed at the center of the bottom plate.

In MPM simulation, elastic material law is used to model the aluminum plate, whose density $\rho = 2.75 \times 10^3$ kg/m^3, the Young's modulus $E = 7.548 \times 10^4$ MPa and the Poisson's ratio $v = 0.33$. In all the numerical studies presented herein, the density of water is chosen as $\rho_w = 1000$ kg/m^3 with corresponding dynamic viscosity $\mu_w = 1.02 \times 10^{-3}$ kg/m s. The effects of surface tension and air flow are ignored in this investigation.

It can be observed from the experiment that before the water column reaches the plate, the front-end shape of water block changes to approximate hemisphere (as shown in Fig. 9(a)). Edahiro's experiments showed that the front-end shape had a significant effect on the impact pressure result [60]. Consequently, the initial shape (Fig. 9(b)) of the water droplet in the MPM simulation was changed to a cylinder with a hemispherical nose (Fig. 9(c)) under

Table 1
MPM simulation of the water block dropping test.

	Particles	Time step (s)	Peak pressure (kPa)	Error
Experiment	–	–	100.4	–
Model-1	17,884	5.91×10^{-7}	98.8	1.59%(−)
Model-2	17,910	5.91×10^{-7}	101.9	1.49%(+)

the premise that the equivalent model (Fig. 9(c)) has the same mass. Two equivalent models are studied here. The first model assumes $r = R$ so that $r = 50$ mm and $h = 66.67$ mm. The second model assumes $r + h = H$ so that $r = 55.37$ mm and $h = 44.63$ mm, where R and H are the original radius and height of the cylindrical water block respectively, r and h denote the equivalent radius and height respectively. In the present simulation, we do not simulate the dropping process, but the simulation starts when the water droplet reaches just above the plate (as shown in Fig. 9(d)) with an initial impact velocity of $v_0 = \sqrt{2gH_0} = 3.1321$ m/s, where the local gravity $g = 9.8$ m/s^2.

Table 1 lists the peak pressure obtained by MPM simulation for the two models described above while Fig. 10 plots the time history of pressure $p(t)$ and the pressure impulse

$$P(t) = \int_0^t p(\tau)d\tau \tag{46}$$

at the center of the plate. They indicate that MPM results are in good agreement with the experimental results. This reveals that the improved MPM is capable of predicting liquid impact pressure. However, high frequency pressure oscillations can be observed from Fig. 10(a), which is a common issue caused by the weakly compressible EOS used for the simulation of incompressible fluid.

4.2. Impact pressure of sloshing fluid

To further investigate the performance of the improved MPM in sloshing simulation, several sloshing experiments were conducted using a rectangular tank of dimensions 1800 mm × 1700 mm × 1000 mm subjected to a harmonic sway or roll excitation at prescribed frequencies. The sloshing experiment setup and the water tank are shown in Fig. 11(a). The tank wall is made of polyvinyl chloride (PVC). The experimental tank was fixed on a moving platform driven by a motor. The center of rotation coincides with the geometric center of the tank as shown in Fig. 11(b). The moving system was designed strong enough to ensure that the sloshing water inside the tank had a small effect on the tank motion. In order to record the time history of pressure, a total of nine pressure sensors which were inserted in holes on the side wall of the tank were used as illustrated in Fig. 11(c). The pressure sensors used in the experiments are KYOWA PGMC-A-200KP with a range of

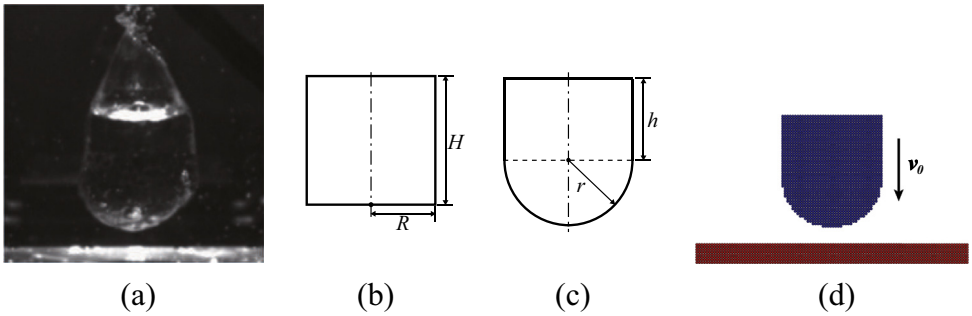

Fig. 9. Initial shape of the water block observed from experiment [60] and the MPM discretization.

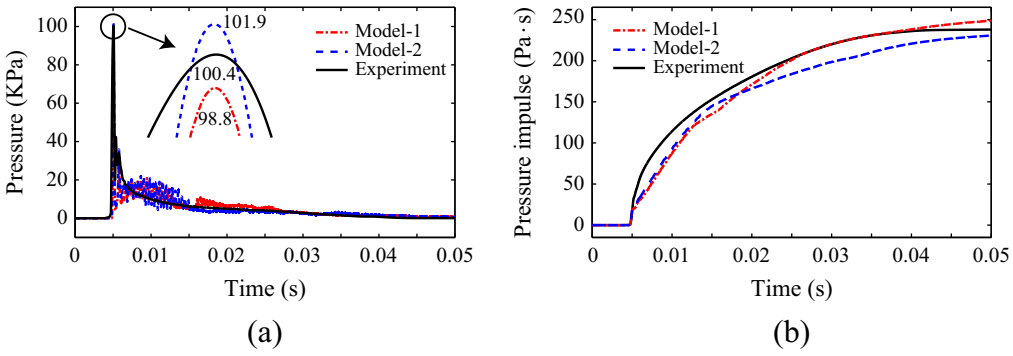

Fig. 10. Results comparison for the water block dropping test: (a) pressure; (b) pressure impulse.

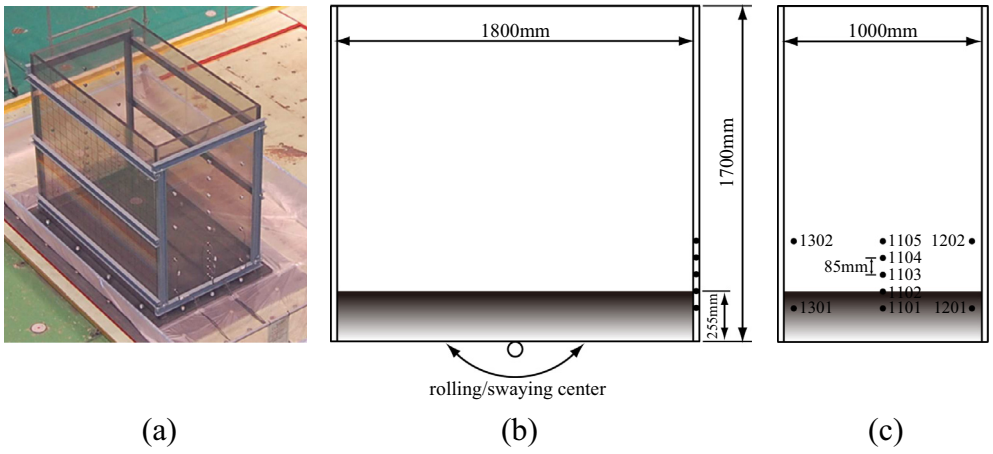

Fig. 11. (a) The experimental platform, (b) front view, (c) side view.

Table 2
Description of the experiment conditions and MPM simulations.

	Motion type	Amplitude	Filling level (%)	Exciting frequency (Hz)	Time step (s)
Case1	Roll	0.75°	15	0.4255	5.5×10^{-5}
Case2	Roll	1.5°	15	0.4255	5.5×10^{-5}
Case3	Sway	36 mm	15	0.4255	5.5×10^{-5}

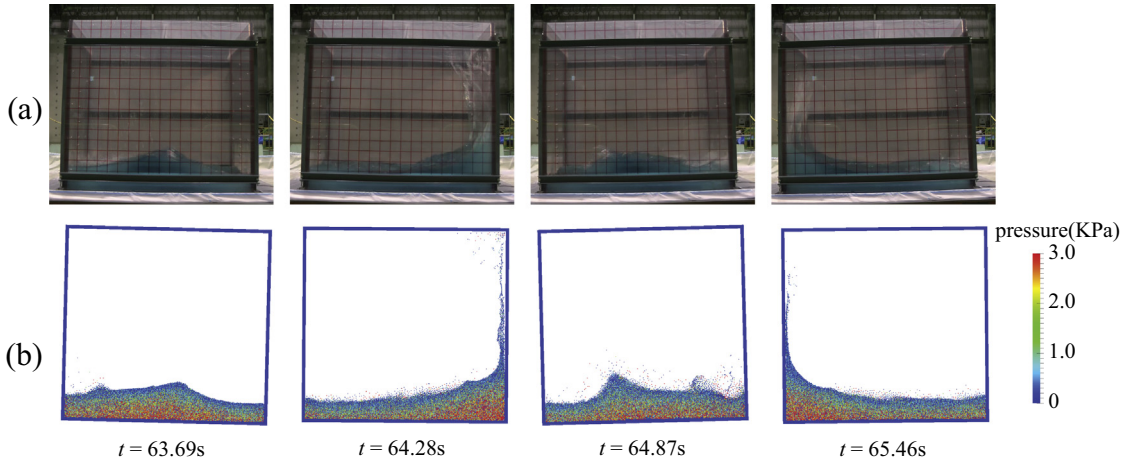

Fig. 12. Snapshots of the inner sloshing water in the rolling tank within a typical cycle. (a) Experimental observations. (b) Particle distributions and pressure fields obtained with MPM.

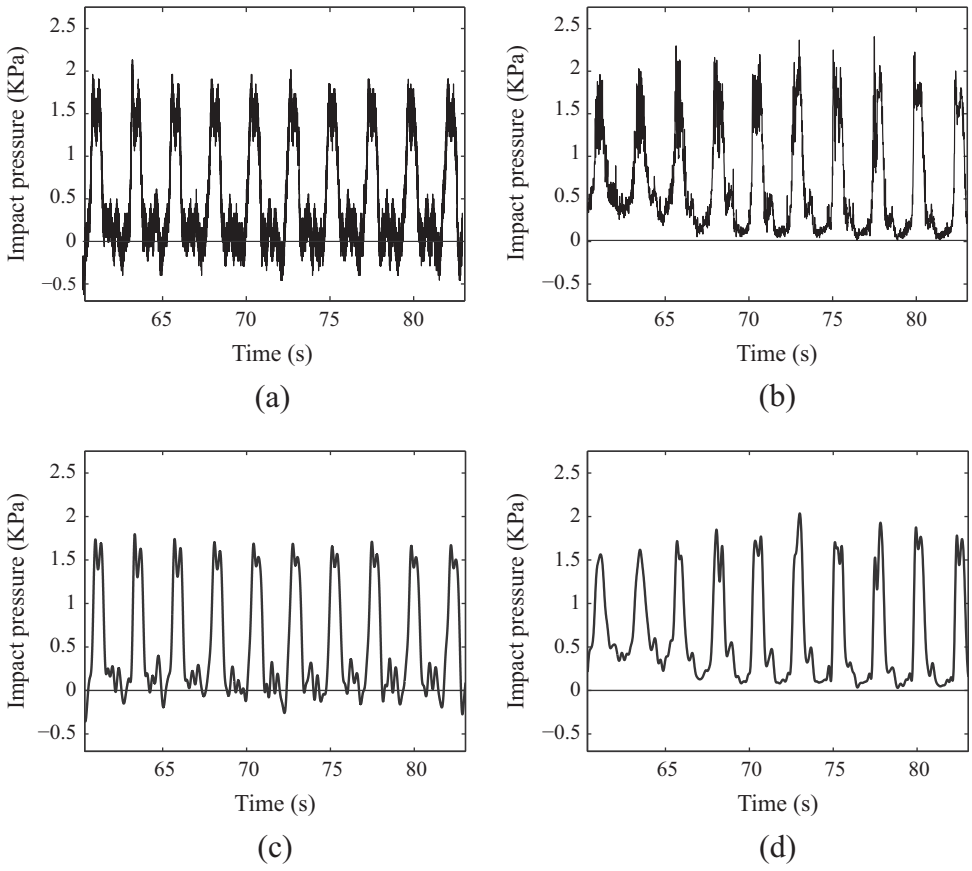

Fig. 13. Time history of impact pressure of Case 1 at gauge 1101: (a) original experimental result; (b) original MPM result; (c) filtered experimental result; (d) filtered MPM result.

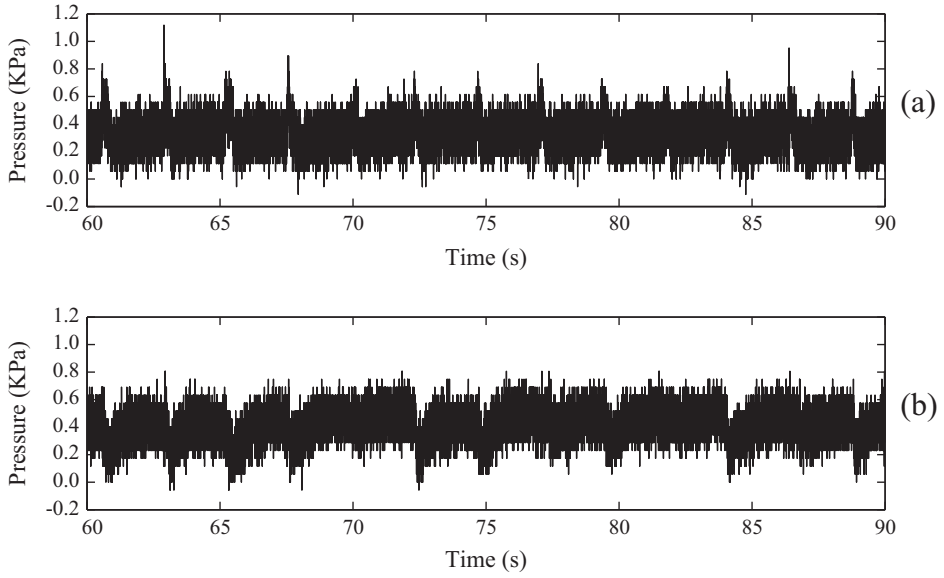

Fig. 14. Experimental results of Case1: (a) gauge 1104 and (b) gauge 1105.

200 KPa. The sampling frequency was 1024 Hz while the sampling interval was 9.76562×10^{-4} s.

For all sloshing cases, the inner fluid is water and the liquid filling level is 255 mm, which is 15% of the total height of the tank. Three different harmonic tank motions were carried out herein. In the first two cases, the tank was allowed to rotate around the transverse axis hence a pitch motion of the rectangular tank was studied. The external excitation can be described as $\alpha(t) = \alpha_0 \sin(\omega_r t + \theta_0)$ with different rotation amplitudes 0.75° and 1.5° respectively. In the third case, the water tank moved under a external sway excitation of $s(t) = s_0 \sin(\omega_s t + \theta_0)$ with a horizontal excitation amplitude of $s_0 = 36$ mm. The frequency of the external

excitation was set to 0.4255 Hz in all cases. Table 2 summarizes the test conditions of the three different experiments and MPM simulations. The initial particle space in MPM was set to 5 mm and 215,232 particles were used with a time step of 5.5×10^{-5} s approximately.

When the amplitude of an external excitation is very large or its frequency is close to the natural frequency of the liquid sloshing system, the liquid inside the container can exhibit violent oscillations thus exert strong impact load on the container. The ith natural sloshing frequency of the fluid motion in a rectangular tank obtained by linear theory [2] is given as

$$f_i = \sqrt{g \frac{i}{4\pi l} \tanh\left(\frac{h}{l}\pi i\right)} \tag{47}$$

where h is the water depth, l is the length of the tank, g is the gravitational acceleration and i is the mode number. For all cases listed in Table 2two values are adopted: $h = 255$ mm and $l = 1800$ mm, therefore the fundamental frequency ($i = 1$) of this sloshing system is $f_n = 0.4255$ Hz. Note that the excitation frequency in these three experiments coincides exactly with the fundamental frequency of the sloshing system.

Liquid sloshing in a moving rectangular tank can be simplified as a two-dimensional liquid flow if the tank width is much smaller than its breadth. Therefore, in order to reduce the MPM computational cost, a limited width (40 mm) of the tank was designed to keep the flow as two-dimensional as possible when the motion is approximately contained in the plane of its two largest dimensions.

In our experiments, the measurements of transient impact pressures were typically 90s long. The stable stage generally occurred after 60s when the inner water was fully excited. Typical sloshing behavior was then repeated with a periodic beating effect. Fig. 12 shows the flow pattern of sloshing liquid at four specific time instants within one period for Case 2. MPM can effectively capture the flow dynamics associated with the changing and breaking free surfaces. Pictures obtained from the MPM simulation show close agreement with the experimental ones. At the beginning of a typical cycle, water particles run up along the right wall and impact onto the right and top side of the tank when the water tank

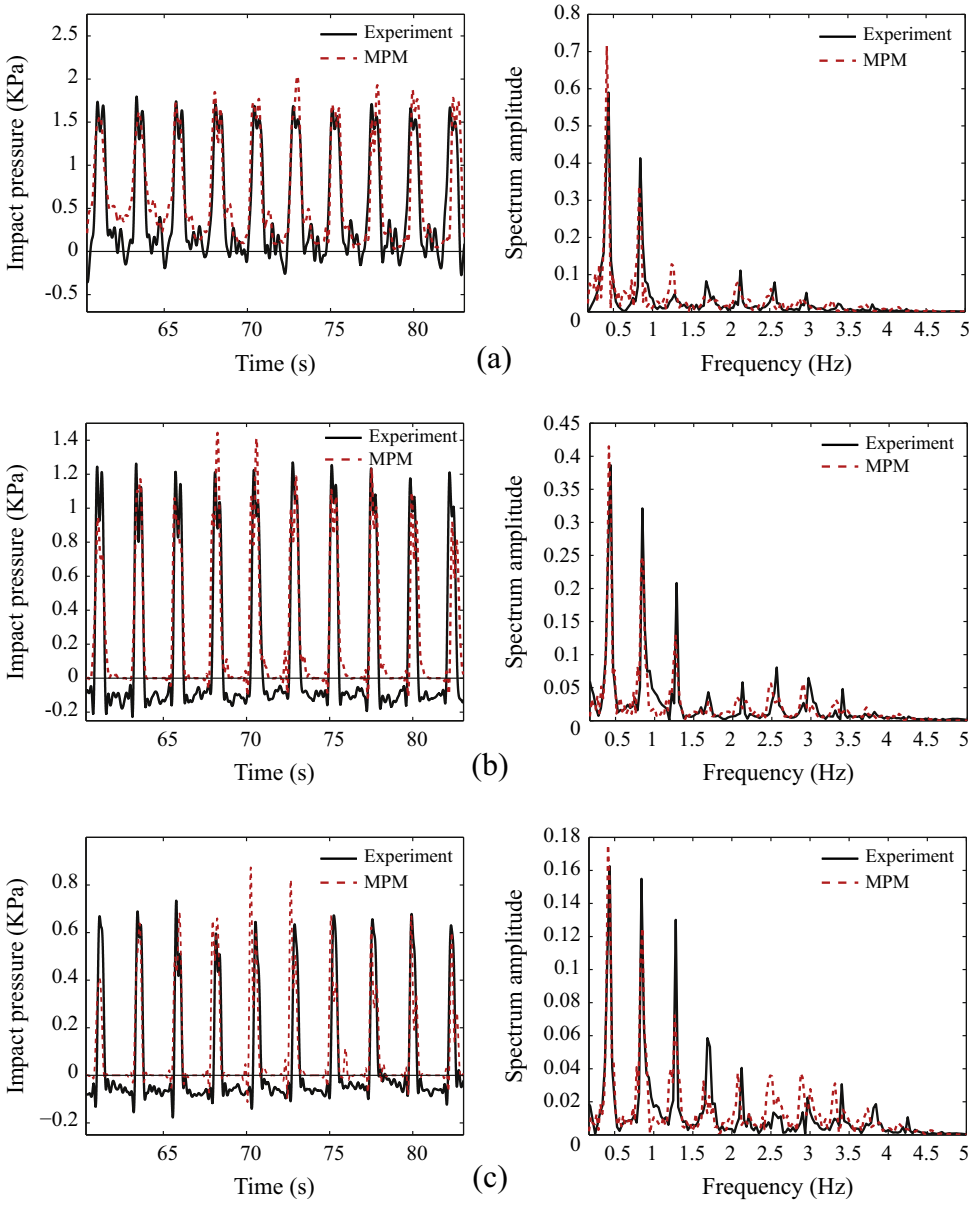

Fig. 15. Impact pressure obtained by experiment and MPM for roll case 1. Left column: time domain; Right column: frequency domain: (a) gauge ID: 1101; (b) gauge ID: 1102; (c) gauge ID: 1103.

is approaching positions with maximum rolling angle with some particles splashed away from the bulky water. Water particles then fall downwards and propagate leftwards with some splashed water particles falling onto the bulky water. With the leftward propagating movement of water, a number of surge fronts appear depending on the geometry and angular velocity of the water tank as well as water height. Later, water particles aggregate and run up along the left wall and then impact onto the left and top side of the tank also with some particles splashed away from the bulky water. As such one period ends followed by similar flow patterns during the next period.

In particle methods with an EOS, small density fluctuations always cause significant unphysical high-frequency pressure oscillations if special care is not taken. Since the water is treated as a weakly compressible fluid with an artificial EOS, which may leads to an unphysical compressibility of the fluid particles in MPM results. The pressure field obtained from MPM are therefore not smooth as shown in Fig. 12(b). Performing a filter over the density of particles provides a feasible technique to further smooth the pressure field.

Fig. 13(a) and (b) compare the time history of impact pressure of Case 1 at gauge 1101 obtained from the experiment and MPM simulation, respectively. Obvious high frequency noises are observed in both experimental and MPM results. To filter out these high frequency noises, a low-pass filter based on the FFT algorithm with a cutoff frequency of 5 Hz is employed and the filtered results are shown in Fig. 13(c) and (d).

It can be observed from the experiments that when the hight of pressure sensor increases, less water run up to the sensor location and the impact pressure obtained from the sensor become smaller. Since the gauge points 1104 and 1105 were initially located 170 mm and 255 mm above the still water level, as shown in Fig. 11(c), impact pressure recorded by these two sensors in experiments were small and drowned out by the signal noises [61,62] as

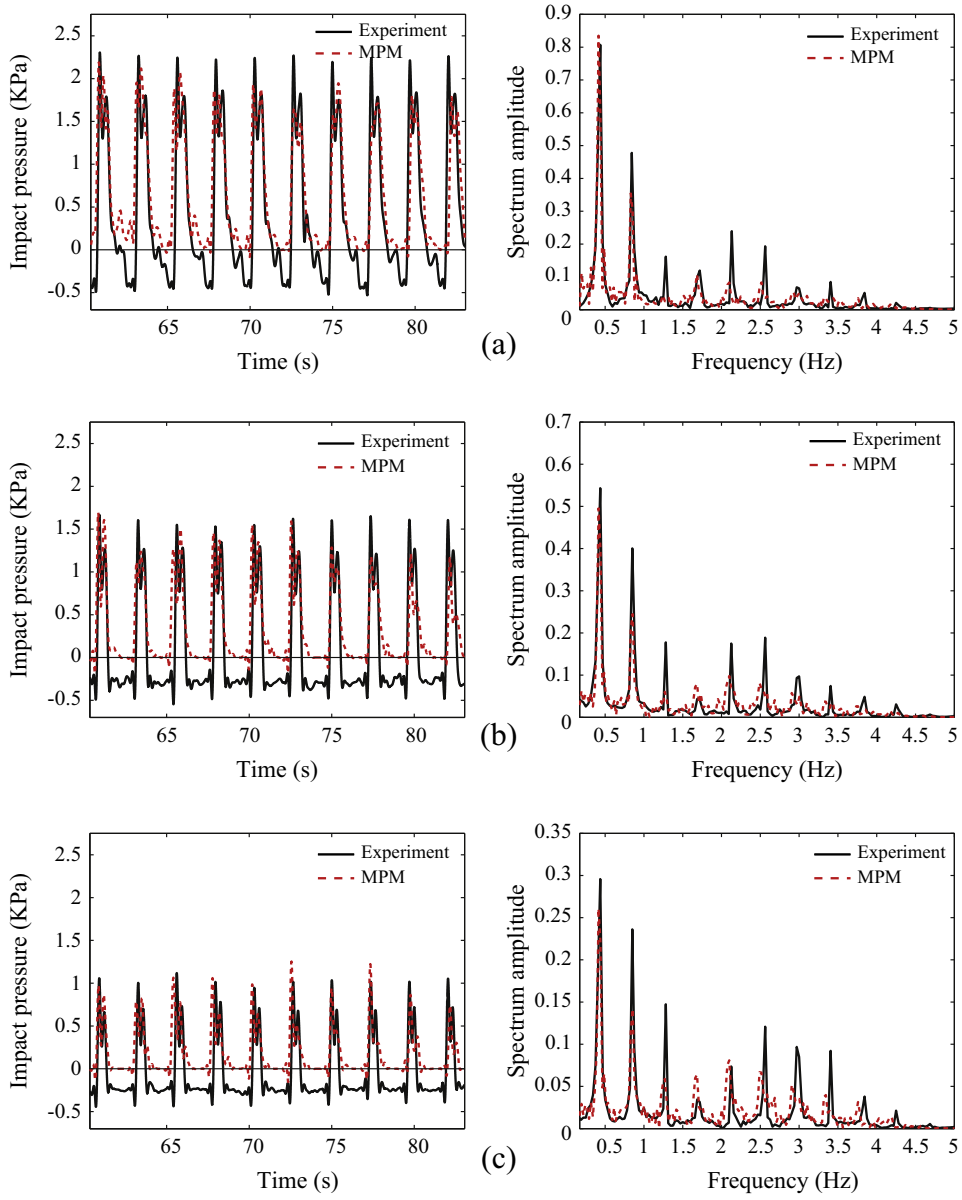

Fig. 16. Impact pressure obtained by experiment and MPM for roll case. Left column: time domain; Right column: frequency domain: (a) gauge ID: 1101; (b) gauge ID: 1102; (c) gauge ID: 1103.

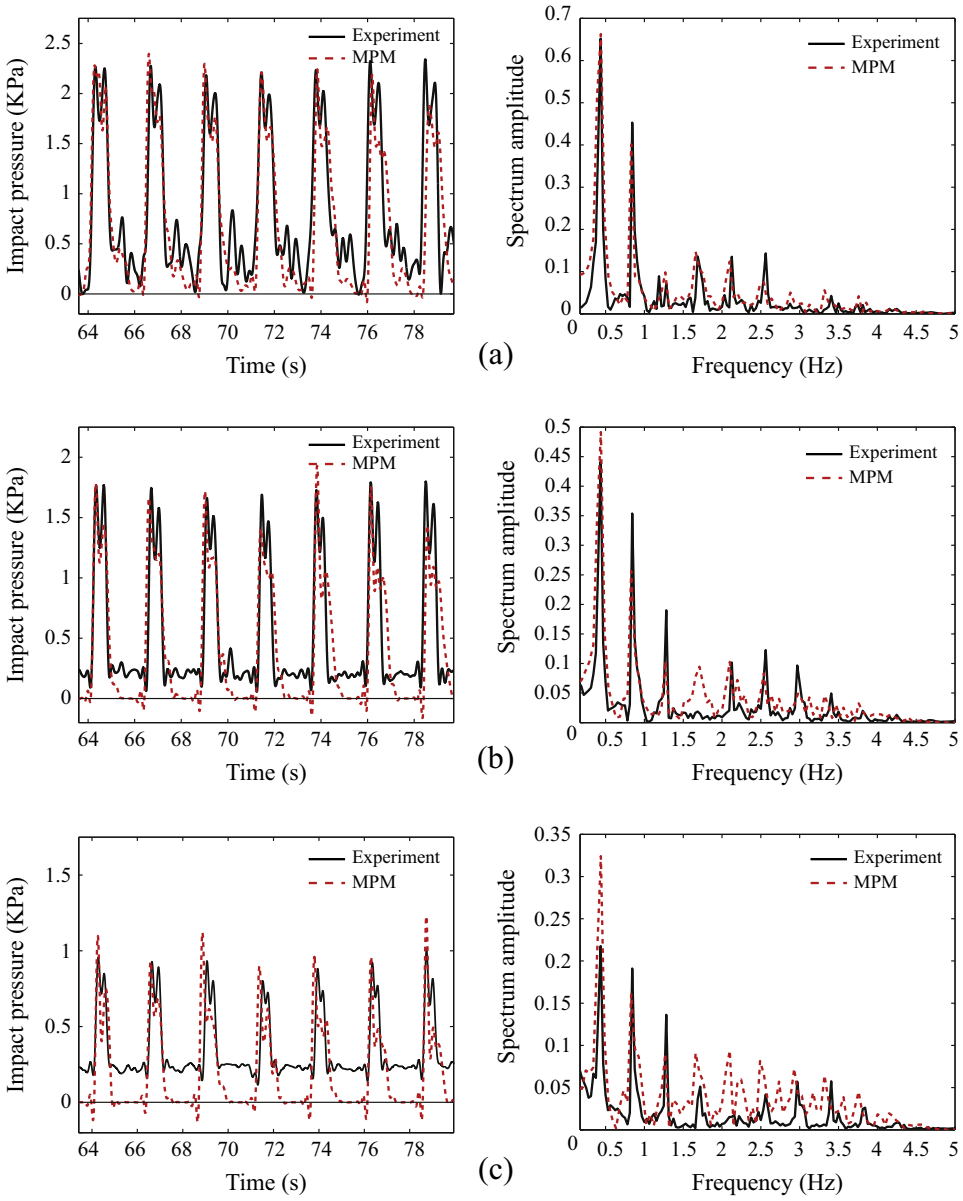

Fig. 17. Impact pressure obtained by MPM and experiment for swaying case. Left column: time domain; Right column: frequency domain: (a) gauge ID: 1101; (b) gauge ID: 1102; (c) gauge ID: 1103.

shown in Fig. 14. For this reason, only the pressure obtained from the gauge points 1101, 1102 and 1103 are chosen for results comparison between experiment and MPM simulation in this paper.

As mentioned previously, the excitation frequency is exactly equal to the fundamental frequency of fluid motion in the experimental tank, the phenomenon of second impact can be observed and two successive peaks in each period of the pressure curves (see Figs. 15–17) are always recorded in both experimental observations and MPM simulations. The reason for this particular feature is that the water movement cannot catch up with the tank's rolling/swaying in this stage. When the tank has reached the maximum amplitude and is moving back toward the equilibrium position, the rest of the fluid reaches the side wall of the tank and produces a second impact (shown in Fig. 12) showing as the double peaks within each period in the pressure curves.

The slosh-induced impact pressures on the tank wall obtained by the MPM simulations and experiments for all three cases are presented in both time domain and frequency domain in Figs. 15–17, respectively. These figures show that the impact pressures obtained by the MPM simulations are in good agreement with the experimental data in both time domain and frequency domain. The magnitudes of the recorded impact pressure generally decrease with the increase of height of the pressure sensor. Moreover, due to the suction on the rigid tank wall caused by the high velocity of air and water at the interface the impact pressure has negative peaks in the experimental results. However, in our numerical scheme, only impact pressure is calculated so there is no negative pressure in MPM simulation results.

In summary, by examining the impact pressure in both time domain and frequency domain, it is revealed that by use of MPM simulation, high accuracy impact pressure of sloshing liquid can be obtained.

5. Conclusions

In this paper, the MPM is extended to model the dynamic behavior of sloshing liquid. The improved MPM includes

corrections of the impact pressure calculation, enhancement in the sloshing loads assignment and incorporation of a weakly compressible equation of state. The accuracy is verified by simulating a water block dropping onto an aluminum plate. The comparisons between the MPM results and experimental results available in the literature show satisfactory agreements.

To further validate the improved MPM in the prediction of liquid sloshing dynamics, several sloshing experiments were conducted. The numerical investigation indicates that the improved MPM can well capture the sloshing phenomenon related to splashing, breaking surfaces and the second impact on the side wall. The MPM with weakly compressible EOS can effectively resolve the flow pattern and violent impact on the solid walls of water tank. The numerical results are in good agreement with the experimental observations both in time domain and frequency domain showing the feasibility and accuracy of applying MPM to sloshing simulations.

However, the weakly compressible EOS used in MPM leads to an unphysical compressibility of the fluid particles thus oscillations appear in the time history of impact pressure. Further improvements for MPM are required to eliminate the unphysical compressibility and pressure oscillations.

References

[1] Ibrahim RA, Pilipchuck VN, Ikeda T. Recent advances in liquid sloshing dynamics. Appl Mech Rev 2001;54(2):133–99.
[2] Faltinsen OM, Timokha AN. Sloshing. Cambridge University Press; 2009.
[3] Ibrahim RA. Liquid sloshing dynamics: theory and applications. Cambridge University Press; 2005.
[4] Valtinsen OM. A nonlinear theory of sloshing in rectangular tanks. J Ship Res 1974;18(4):224–41.
[5] Faltinsen OM. A numerical nonlinear method of sloshing in tanks with two-dimensional flow. J Ship Res 1978;22(3):193–202.
[6] Faltinsen OM, Rognebakke OF, Lukovsky IA, Timokha AN. Multidimensional modal analysis of nonlinear sloshing in a rectangular tank with finite water depth. J Fluid Mech 2000;407:201–34.
[7] Faltinsen OM, Timokha AN. On sloshing modes in a circular tank. J Fluid Mech 2012;695:467–77.
[8] Akyildiz H, Unal E. Experimental investigation of pressure distribution on a rectangular tank due to the liquid sloshing. Ocean Eng 2005;32(11–12):1503–16.
[9] Yung TW, Ding Z, He H, Sandstrom RE. LNG sloshing: characteristics and scaling laws. Int J Offshore Polar Eng 2009;19(4):264–70.
[10] Scardovelli R, Zaleski S. Direct numerical simulation of free-surface and interfacial flow. Ann Rev Fluid Mech 1999;31(1):567–603.
[11] Cariou A, Casella G. Liquid sloshing in ship tanks: a comparative study of numerical simulation. Mar Struct 1999;12(3):183–98.
[12] Rebouillat S, Liksonov D. Fluid-structure interaction in partially filled liquid containers: a comparative review of numerical approaches. Comput Fluids 2010;39(5):739–46.
[13] Kim Y. Numerical simulation of sloshing flows with impact load. Appl Ocean Res 2001;23(1):53–62.
[14] Chen BF, Nokes R. Time-independent finite difference analysis of fully non-linear and viscous fluid sloshing in a rectangular tank. J Comput Phys 2005;209(1):47–81.
[15] Muzaferija S, Peric M. Computation of free-surface flows using the finite-volume method and moving grids. Numer Heat Transf 1997;32(4):369–84.
[16] Wang JP, Borthick AGL, Taylor RE. Finite-volume-type VOF method on dynamically adaptive quadtree grids. Int J Numer Methods Fluids 2004;45(5):485–508.
[17] Wu GX, Ma QW, Eatock Taylor R. Numerical simulation of sloshing waves in a 3D tank based on a finite element method. Appl Ocean Res 1998;20(6):337–55.
[18] Mitra S, Upadhyay PP, Sinhamahapatra KP. Slosh dynamics of inviscid fluids in two-dimensional tanks of various geometry using finite element method. Int J Numer Methods Fluids 2008;56(9):1625–51.
[19] Liu DM, Lin PZ. A numerical study of three-dimensional liquid sloshing in tanks. J Comput Phys 2008;227(8):3921–39.
[20] Veldman AEP, Gerrits J, Luppes R, Helder JA, Vreeburg JPB. The numerical simulation of liquid sloshing on board spacecraft. J Comput Phys 2007;224(1):82–99.
[21] Fang ZY, Duan MY, Zhu RQ. Numerical simulation of liquid sloshing in a liquid tank based on level-set method. J Ship Mech 2007;11(1):62–7.
[22] Idelsohn SR, Onate E, Del Pin F. The particle finite element method: a powerful tool to solve incompressible flows with free-surfaces and breaking waves. Int J Numer Methods Eng 2004;61(7):964–89.
[23] Koshizuka S, Nobe A, Oka Y. Numerical analysis of breaking waves using the moving particle semi-implicit method. Int J Numer Methods Fluids 1998;26(7):751–69.
[24] Lee BH, Park JC, Kim MH, Hwang SC. Step-by-step improvement of MPS method in simulating violent free-surface motions and impact-loads. Comput Methods Appl Mech Eng 2011;200(9–12):1113–25.
[25] Nestor RM, Basa M, Lastiwka M, Quinlan NJ. Extension of the finite volume particle method to viscous flow. J Comput Phys 2009;228(5):1733–49.
[26] Liu GR, Liu MB. Smoothed particle hydrodynamics: a meshfree particle method. World Scientific Publishing Company; 2003.
[27] Gingold RA, Monaghan JJ. Smoothed particle hydrodynamics-theory and application to non-spherical stars. Mon Notices Roy Astron Soc 1977;181:375–89.
[28] Libersky LD, Petschek AG, Carney TC, Hipp JR, Allahdadi FA. High strain Lagrangian hydrodynamics: a three-dimensional SPH code for dynamic material response. J Comput Phys 1993;109(1):67–75.
[29] Swegle JW, Attaway SW. On the feasibility of using smoothed particle hydrodynamics for underwater explosion calculations. Comput Mech 1995;17(3):151–68.
[30] Liu MB, Liu GR, Zong Z, Lam KY. Computer simulation of high explosive explosion using smoothed particle hydrodynamics methodology. Comput Fluids 2003;32(3):305–22.
[31] Johnson GR, Beissel SR. Normalized smoothing functions for SPH impact computations. Int J Numer Methods Eng 1996;39(16):2725–41.
[32] Hu XY, Adams NA. An incompressible multi-phase SPH method. J Comput Phys 2007;227(1):264–78.
[33] Rodriguez-Paz M, Bonet J. A corrected smooth particle hydrodynamics formulation of the shallow-water equations. Comput Struct 2005;83(17):1396–410.
[34] Bockmann A, Shipilova O, Skeie G. Incompressible SPH for free surface flows. Comput Fluids 2012;67:138–51.
[35] Souto-Iglesias A, Delorme L, Perez-Rojas L, Abril-Perez S. Liquid moment amplitude assessment in sloshing type problems with smooth particle hydrodynamics. Ocean Eng 2006;33(11):1462–84.
[36] Anghileri M, Castelletti LML, Tirelli M. Fluid-structure interaction of water filled tanks during the impact with the ground. Int J Impact Eng 2005;31(3):235–54.
[37] Monaghan JJ. Simulating free surface flows with SPH. J Comput Phys 1994;110(2):399–406.
[38] Shao JR, Li HQ, Liu GR, Liu MB. An improved SPH method for modeling liquid sloshing dynamics. Comput Struct 2012;100:18–26.
[39] Sigalotti LDG, Lopez H, Trujillo L. An adaptive SPH method for strong shocks. J Comput Phys 2009;228(16):5888–907.
[40] Cummins SJ, Rudman M. An SPH projection method. J Comput Phys 1999;152(2):584–607.
[41] Sulsky D, Chen Z, Schreyer HL. A particle method for history-dependent materials. Comput Methods Appl Mech Eng 1994;118(1–2):179–96.
[42] Sulsky D, Zhou SJ, Schreyer HL. Application of a particle-in-cell method to solid mechanics. Comput Phys Commun 1995;87(1–2):236–52.
[43] Brackbill JU, Ruppel HM. FLIP: a method for adaptively zoned, particle-in-cell calculations in two dimensions. J Comput Phys 1986;65(2):314–43.
[44] Chen Z, Brannon R. An evaluation of the material point method. Report: SAND 482. 87185-0893; 2002.
[45] Gilmanov A, Acharya S. A hybrid immersed boundary and material point method for simulating 3D fluid–structure interaction problems. Int J Numer Methods Fluids 2008;56(12):2151–77.
[46] Hu PG, Xue LP, Mao SL, Kamakoti R, Zhao HW, Dittakavi Z, et al. Material point method applied to fluid–structure interaction (FSI)/aeroelasticity problems. In: 48th AIAA aerospace sciences meeting including the new horizons forum and aerospace exposition; 2010.
[47] York AR, Sulsky D, Schreyer HL. Fluid-membrane interaction based on the material point method. Int J Numer Methods Eng 2000;48(6):901–24.
[48] Sulsky D, Schreyer H, Peterson K, Kwok R, Coon M. Using the material-point method to model sea ice dynamics. J Geophys Res: Oceans (1978–2012) 2007;112(C2):1–18.
[49] Zhang DZ, Zou QS, VanderHeyden WB, Ma X. Material point method applied to multiphase flows. J Comput Phys 2008;227(6):3159–73.
[50] Zhang X, Sze KY, Ma S. An explicit material point finite element method for hyper-velocity impact. Int J Numer Methods Eng 2006;66(4):689–706.
[51] Lian YP, Zhang X, Zhou X, Ma ZT. A FEMP method and its application in modeling dynamic response of reinforced concrete subjected to impact loading. Comput Methods Appl Mech Eng 2011;200(17):1659–70.
[52] Ma S, Zhang X, Qiu XM. Comparison study of MPM and SPH in modeling hypervelocity impact problems. Int J Impact Eng 2009;36:272–82.
[53] Bardenhagen SG, Brackbill JU, Sulsky D. Numerical study of stress distribution in sheared granular material in two dimensions. Phys Rev E 2000;62(3):3882–90.
[54] Bardenhagen SG, Guilkey JE, Roessig KM, Brackbill JU, Witzel WM, Foster JC. An improved contact algorithm for the material point method and application to stress propagation in granular material. Comput Model Eng Sci 2001;2(4):509–22.
[55] Huang P, Zhang X, Ma S, Huang X. Contact algorithms for the material point method in impact and penetration simulation. Int J Numer Methods Eng 2011;85(4):498–517.
[56] Ma ZT, Zhang X, Huang P. An object-oriented MPM framework for simulation of large deformation and contact of numerous grains. Comput Model Eng Sci 2010;55:61–87.
[57] Morris JP, Fox PJ, Zhu Y. Modeling low Reynolds number incompressible flows using SPH. J Comput Phys 1997;136(1):214–26.

[58] Hu W, Chen Z. A multi-mesh MPM for simulating the meshing process of spur gears. Comput Struct 2003;81(20):1991–2002.
[59] Lian YP, Zhang X, Liu Y. Coupling of finite element method with material point method by local multi-mesh contact method. Comput Methods Appl Mech Eng 2011;200(47):3482–94.
[60] Edahiro T. Experimental and numerical analysis of impact pressure of dropping water block (in Japanese). Master's thesis. Tokyo Marine University; 2007.
[61] Pistani F, Thiagarajan K. Experimental measurements and data analysis of the impact pressures in a sloshing experiment. Ocean Eng 2012;52:60–74.
[62] Chen YG, Djidjeli K, Price WG. Numerical simulation of liquid sloshing phenomena in partially filled containers. Comput Fluids 2009;38(4):830–42.